On the complex conjugate roots of the Rayleigh equation: The leaky surface wave

Christoph T. Schröder[a] and Waymond R. Scott, Jr.[b]
School of Electrical and Computer Engineering, Georgia Institute of Technology, Atlanta, Georgia 30332-0250

(Received 24 May 2001; accepted for publication 11 September 2001)

In recent experiments and numerical studies, a leaky surface wave has been observed at the surface of an isotropic homogeneous elastic solid. This paper gives a detailed description of this leaky surface wave and explains its origin from the fundamental differential equations. Theoretically, the leaky surface wave arises from the complex conjugate roots of the Rayleigh equation. The complex conjugate roots give rise to a wave that propagates along the surface and is coupled to a plane shear wave in the medium. Due to the coupling, the surface wave leaks energy into the medium and is highly inhomogeneous. Its particle motion at the surface is prograde in nature, distinguishing it from the well-known Rayleigh surface wave which causes a retrograde particle motion. © *2001 Acoustical Society of America.* [DOI: 10.1121/1.1419085]

PACS numbers: 43.20.Bi, 43.35.Pt, 68.35.Ja [ANN]

I. INTRODUCTION

Elastic surface waves have been the subject of extensive research, since Lord Rayleigh first discovered the existence of elastic waves confined to the superficial region of an infinite homogeneous isotropic solid more than a century ago.[1] Elastic surface waves play an important role in various fields. In seismology, surface waves have been found to carry the bulk of the energy among the waves excited by an earthquake. In electroacoustics, surface waves are utilized to make filters and resonators. In geoscience, the propagation characteristics of surface waves are used to obtain information about the physical properties of the ground. In this paper, the theory of elastic surface waves is revisited.

A point source placed on the surface of a homogeneous isotropic medium excites five different kinds of waves: a pressure wave and a shear wave propagating in the medium, a Rayleigh surface wave that is confined to the surface of the medium, a lateral wave that is induced by the pressure wave at the surface, and a leaky surface wave that travels along the surface with a wave speed smaller than the pressure wave but larger than the shear wave. The first four of these wave types are well-known and have been treated extensively in the literature. However, the existence and theoretical foundation of the leaky surface wave has not been discussed as much.

The leaky surface wave arises from the complex conjugate roots of the Rayleigh equation. The leaky surface wave is an inhomogeneous wave that propagates along the surface with a phase velocity larger than the shear wave but smaller than the pressure wave. It couples into a plane shear wave that propagates in the medium. Due to the coupling, the surface wave loses energy and, thus, decays in its propagation direction.

The leaky surface wave has been observed by various authors in experimental and numerical studies. For example, Roth *et al.* noticed a rapidly decaying seismic surface wave in an environment with a very high Poisson ratio that had a phase velocity larger than the Rayleigh wave, but smaller than the pressure wave.[2] Smith *et al.* identified prograde and retrograde surface wave modes in a geologic study conducted on the shore of the gulf of Mexico.[3] Glass and Maradudin found a leaky surface wave to exist in the flat-surface limit of a corrugated crystal surface.[4] And Phinney provides a theoretical study of the leaky surface wave, which he calls a *Pseudo-P* mode.[5] Although not all of these authors explicitly describe a leaky surface wave, their observations are consistent with the results presented in this paper.

In this paper, the theoretical derivation of the leaky surface wave is described in some detail. In Sec. II, the governing equations are briefly outlined, leading to the Rayleigh equation. In Sec. III, the various roots of the Rayleigh equation are discussed. It will be shown that for materials with a high Poisson ratio a leaky surface wave exists, due to the complex conjugate roots of the Rayleigh equation. In Sec. IV, the waves excited by a line source on the surface are derived analytically. The method of steepest descent is applied to obtain closed-form expressions for the various waves in the far field.

II. THE RAYLEIGH EQUATION

The elastic wave fields at the surface of a semi-infinite, isotropic, lossless, homogeneous half space are to be determined. The half-space is bounded at $z=0$ by a free-surface boundary. The fields are assumed to be invariant in the y-direction and nonzero only in the x-z plane (*plane-strain case*, $u_y=\partial/\partial y=0$). Thus, the originally three-dimensional problem reduces to a two-dimensional one. The elastic wave fields in a medium may be expressed in terms of their potential functions:[6]

$$\mathbf{u}=\nabla\Phi+\nabla\times\mathbf{H}, \tag{1}$$

where $\mathbf{u}$ is the displacement vector, Φ is a scalar potential describing the longitudinal pressure wave, and $\mathbf{H}$ is a vector

[a]Electronic mail: christoph.schroeder@ece.gatech.edu
[b]Electronic mail: waymond.scott@ece.gatech.edu

potential describing the transverse shear wave. The potentials satisfy the wave equations

$$\nabla^2\Phi = \frac{1}{c_P^2}\frac{\partial^2\Phi}{\partial t^2}, \tag{2}$$

$$\nabla^2\mathbf{H} = \frac{1}{c_S^2}\frac{\partial^2\mathbf{H}}{\partial t^2}, \tag{3}$$

for the pressure and shear wave, respectively, with their corresponding wave speeds, c_P and c_S. In the *plane-strain* case, the only nonzero vector potential component is H_y and the only nonzero displacement components are u_x and u_z. The only independent stress components are τ_{xx}, τ_{zz}, and τ_{xz}.

Assuming harmonic time-dependence, the plane wave solutions for Φ and H_y satisfying Eqs. (2) and (3) are given by

$$\Phi = Ae^{j\xi x + j\alpha z - j\omega t}, \tag{4}$$

$$H_y = Be^{j\xi x + j\beta z - j\omega t} \tag{5}$$

and the wave numbers are defined by

$$\alpha^2 = \omega^2/c_P^2 - \xi^2, \tag{6}$$

$$\beta^2 = \omega^2/c_S^2 - \xi^2, \tag{7}$$

$$\xi^2 = \omega^2/c^2. \tag{8}$$

Using the well-known differential equations, the displacement and stress components are obtained:

$$u_x = (j\xi\, Ae^{j\alpha z} - j\beta\, Be^{j\beta z})e^{j\xi x}, \tag{9}$$

$$u_z = (j\alpha\, Ae^{j\alpha z} + j\xi\, Be^{j\beta z})e^{j\xi x}, \tag{10}$$

$$\tau_{xx} = \mu((2\alpha^2 - \beta^2 - \xi^2)Ae^{j\alpha z} + 2\beta\xi\, Be^{j\beta z})e^{j\xi x}, \tag{11}$$

$$\tau_{zz} = \mu((\xi^2 - \beta^2 Ae^{j\alpha z} - 2\beta\xi\, Be^{j\beta z})e^{j\xi x}, \tag{12}$$

$$\tau_{xz} = \mu(-2\alpha\xi\, Ae^{j\alpha z} + (\beta^2 - \xi^2)Be^{j\beta z})e^{j\xi x}. \tag{13}$$

At the surface, the normal stress vanishes, and thus $\tau_{zz}|_{z=0} = \tau_{xz}|_{z=0} = 0$. Using this condition, the ratio of the coefficients is determined from Eqs. (12) and (13) to be

$$\frac{A}{B} = \frac{2\xi\beta}{\xi^2 - \beta^2} = -\frac{\xi^2 - \beta^2}{2\xi\alpha}. \tag{14}$$

Re-inserting the amplitude ratio into Eqs. (12) and (13), the characteristic equation is obtained:

$$(\xi^2 - \beta^2)^2 + 4\xi^2\alpha\beta = 0. \tag{15}$$

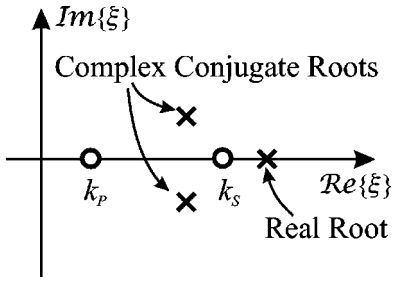

FIG. 1. Schematical arrangement of the roots in the complex ξ-plane.

Equation (15) is commonly called the *Rayleigh Equation*, because it gives rise to the well-known Rayleigh surface wave.

Using Eqs. (6)–(8), the characteristic equation can be rewritten in terms of the wave speeds:

$$\left(2 - \frac{c^2}{c_S^2}\right)^2 + 4\sqrt{\frac{c^2}{c_P^2} - 1}\sqrt{\frac{c^2}{c_S^2} - 1} = 0. \tag{16}$$

By rationalizing, this equation may be expressed as

$$\left(\frac{c}{c_S}\right)^2\left(\left(\frac{c}{c_S}\right)^6 - 8\left(\frac{c}{c_S}\right)^4 + (24 - 16(c_S/c_P)^2)\left(\frac{c}{c_S}\right)^2 - 16(1 - (c_S/c_P)^2)\right) = 0. \tag{17}$$

Equation (17) always has three solutions for c^2 (when neglecting the trivial solution). Dependent on the Poisson Ratio ν of a material, different kinds of roots arise. For $\nu < 0.263$, Eq. (17) has three real roots. For $\nu > 0.263$, Eq. (17) has one real root and two complex conjugate roots. In each case, the real root that is smallest in magnitude gives rise to the Rayleigh surface wave, which propagates along the surface and decays into the medium. The other roots have often been classified as erroneous or nonphysical roots of the Rayleigh equation.[6–8] However, it will be shown here that the complex conjugate roots of the Rayleigh equation in fact give rise to a *leaky surface wave*.

III. THE ROOTS OF THE RAYLEIGH EQUATION

Let the roots of Eq. (17) be denoted by c. In general, c will be complex:

$$c = c_r + jc_i, \tag{18}$$

TABLE I. Solutions to the Rayleigh equation.

(1)	$\xi_r > 0,\ \xi_i = 0$	$\alpha_r = 0, \alpha_i > 0$ $\Phi \sim e^{-\lvert\alpha_i\rvert z} e^{j\lvert\xi_r\rvert x}$	$\beta_r = 0, \beta_i > 0$ $H_z \sim e^{-\lvert\beta_i\rvert z} e^{j\lvert\xi_r\rvert x}$
(2)	$\xi_r > 0,\ \xi_i < 0$	$\alpha_r > 0, \alpha_i > 0$ $\Phi \sim e^{(j\lvert\alpha_r\rvert - \lvert\alpha_i\rvert)z} e^{(j\lvert\xi_r\rvert + \lvert\xi_i\rvert)x}$	$\beta_r < 0, \beta_i < 0$ $H_z \sim e^{(-j\lvert\beta_r\rvert + \lvert\beta_i\rvert)z} e^{(j\lvert\xi_r\rvert + \lvert\xi_i\rvert)x}$
(3)	$\xi_r > 0,\ \xi_i > 0$	$\alpha_r < 0, \alpha_i > 0$ $\Phi \sim e^{(-j\lvert\alpha_r\rvert - \lvert\alpha_i\rvert)z} e^{(j\lvert\xi_r\rvert - \lvert\xi_i\rvert)x}$	$\beta_r > 0, \beta_i < 0$ $H_z \sim e^{(j\lvert\beta_r\rvert + \lvert\beta_i\rvert)z} e^{(j\lvert\xi_r\rvert - \lvert\xi_i\rvert)x}$
(4)	$\xi_r > 0,\ \xi_i < 0$	$\alpha_r < 0, \alpha_i < 0$ $\Phi \sim e^{(-j\lvert\alpha_r\rvert + \lvert\alpha_i\rvert)z} e^{(j\lvert\xi_r\rvert + \lvert\xi_i\rvert)x}$	$\beta_r > 0, \beta_i > 0$ $H_z \sim e^{(j\lvert\beta_r\rvert - \lvert\beta_i\rvert)z} e^{(j\lvert\xi_r\rvert + \lvert\xi_i\rvert)x}$
(5)	$\xi_r > 0,\ \xi_i > 0$	$\alpha_r > 0, \alpha_i < 0$ $\Phi \sim e^{(j\lvert\alpha_r\rvert + \lvert\alpha_i\rvert)z} e^{(j\lvert\xi_r\rvert - \lvert\xi_i\rvert)x}$	$\beta_r < 0, \beta_i > 0$ $H_z \sim e^{(-j\lvert\beta_r\rvert - \lvert\beta_i\rvert)z} e^{(j\lvert\xi_r\rvert - \lvert\xi_i\rvert)x}$

TABLE II. Solutions to the Rayleigh equation.

	$\xi=$	$\alpha=$	$\beta=$
(1)	$2.5998k_P$	$j2.3997k_P$	$j0.8711k_P$
(2)	$(1.2184-j0.2526)k_P$	$(0.4030+j0.7636)k_P$	$(-2.1448-j0.1435)k_P$
(3)	$(1.2184+j0.2526)k_P$	$(-0.4030+j0.7636)k_P$	$(2.1448-j0.1435)k_P$
(4)	$(1.2184-j0.2526)k_P$	$(-0.4030-j0.7636)k_P$	$(2.1448+j0.1435)k_P$
(5)	$(1.2184+j0.2526)k_P$	$(0.4030-j0.7636)k_P$	$(-2.1448+j0.1435)k_P$

where c_r is the real part and c_i is the imaginary part of c. If c is purely real ($c=c_r$), ξ will be real [see Eq. (8)]. If additionally c is smaller than both the pressure wave speed and the shear wave speed, i.e., $c=c_r<c_S<c_P$, α and β will be purely imaginary. For the solution to be physical, $\mathrm{Im}\{\alpha\}=\alpha_i>0$ and $\mathrm{Im}\{\beta\}=\beta_i>0$, thus the waves described by these wave numbers *propagate* in the *x*-direction and *decay* in the *z*-direction. This solution represents the well-known Rayleigh surface wave, first explored by Lord Rayleigh more than a century ago.[1] A solution of this form always exists, independent of the Poisson ratio of a material.

For $\nu<0.263$, two more purely real roots of the Rayleigh equation exist. It can be shown that for these roots the wave speed is always larger than the pressure wave speed, c_P. These two roots describe the angles of incidence at which *complete mode conversion* occurs. In the case of complete mode conversion an incident shear wave, for example, is completely reflected as a pressure wave, without inducing a reflected shear wave component. Complete mode conversion is physically possible only for materials with a Poisson ratio smaller than 0.263 and occurs at two distinct angles of incidence, defined by the two roots of the Rayleigh equation (see also, for example, Graff[6]).

If $\nu>0.263$, one real root and two complex conjugate roots of the Rayleigh equation arise. The real root again gives rise to the Rayleigh surface wave. For the complex conjugate roots, the wave speed is complex, $c=c_r+jc_i$, and consequently also the wave numbers are complex: $\xi=\xi_r+j\xi_i$, $\alpha=\alpha_r+j\alpha_i$ and $\beta=\beta_r+j\beta_i$. It can be shown that for the complex conjugate roots the real part of the wave speed is always smaller than the pressure wave speed, but larger than the shear wave speed, $c_S<\mathrm{Re}\{c\}<c_P$.

Although c may be a solution to Eq. (17), it does not necessarily follow that also Eq. (15) is fulfilled. This is due to the manipulation of Eq. (15) to arrive at Eq. (17). In fact, the complex conjugate roots of Eq. (17) do not represent solutions to Eq. (16). It can be shown, however, that they do represent solutions to Eq. (15), if the signs of the wave numbers α and β are picked correctly. It may be recalled that according to Eqs. (6) and (7) the wave numbers α and β are functions of the square root of c^2,

$$\alpha=\pm\frac{\omega}{c}\sqrt{\frac{c^2}{c_P^2}-1}=\pm(\alpha_r+j\alpha_i), \tag{19}$$

$$\beta=\pm\frac{\omega}{c}\sqrt{\frac{c^2}{c_S^2}-1}=\pm(\beta_r+j\beta_i). \tag{20}$$

The sign in front of the square roots must be chosen according to physical and causal constraints of the underlying problem. To obtain Eq. (16), the positive sign has been assumed for both α and β. However, it turns out that Eq. (15) is only satisfied if, for the complex conjugate roots, both the real part and the imaginary part of α and β have opposite signs, i.e., $\mathrm{sign}(\alpha_r)\neq\mathrm{sign}(\beta_r)$ and $\mathrm{sign}(\alpha_i)\neq\mathrm{sign}(\beta_i)$.

Figure 1 shows schematically the arrangement of the roots in the complex ξ-plane. The possible solutions of the Rayleigh equation are summarized in Table I, giving all possible combinations of ξ, α and β. Only waves propagating in the positive *x*-direction are considered. Five possible solutions arise.

The first solution describes the Rayleigh surface wave. For the second solution, both the pressure wave potential and the shear wave potential, Φ and H_y, propagate and increase in the positive *x*-direction ($\xi_r>0$, $\xi_i<0$). However, Φ propagates and decays in the positive *z*-direction ($\alpha_r>0$, $\alpha_i>0$), whereas H_y propagates and decays in the negative *z*-direction ($\beta_r<0$, $\beta_i<0$). For the third solution, the potentials decay in the *x*-direction ($\xi_i>0$). Φ now propagates and increases in the negative *z*-direction ($\alpha_r<0$, $\alpha_i>0$), whereas H_y propagates and increases in the positive *z*-direction ($\beta_r>0$, $\beta_i<0$). For the fourth and fifth solution, the signs of α and β are reversed.

The behavior of the five possible solutions is best demonstrated by calculating the wave fields for a medium with a specific value of Poisson's ratio. Assuming Poisson's ratio to be $\nu=0.4$, the elastic wave fields are computed using Eqs. (9)–(13). The amplitude of the shear wave potential is chosen to be unity, and the amplitude of the pressure wave potential is computed with Eq. (14). For $\nu=0.4$, the pressure wave speed exceeds the shear wave speed by a factor of about 2.45: $c_P=2.4495c_S$. The roots of Eq. (17) in terms of the shear wave speed c_S are

$$c=\begin{cases}0.9422c_S\\(1.9276+j0.3996)c_S\\(1.9276-j0.3996)c_S.\end{cases} \tag{21}$$

The resulting wave numbers are shown in Table II. All wave numbers are expressed in terms of the longitudinal wave number, $k_P=\omega/c_P$.

In Fig. 2, the displacements according to the five solutions of the Rayleigh equation are plotted versus *x* and *z*. The distance on the axes is normalized to the wavelength of the Rayleigh surface wave, λ_R. The two columns show the horizontal and vertical displacements, u_x and u_z. Pseudo-color plots are used to display the wave fields, employing a logarithmic scale with a dynamic range of 50 dB. Superimposed with the horizontal displacement component is the real part

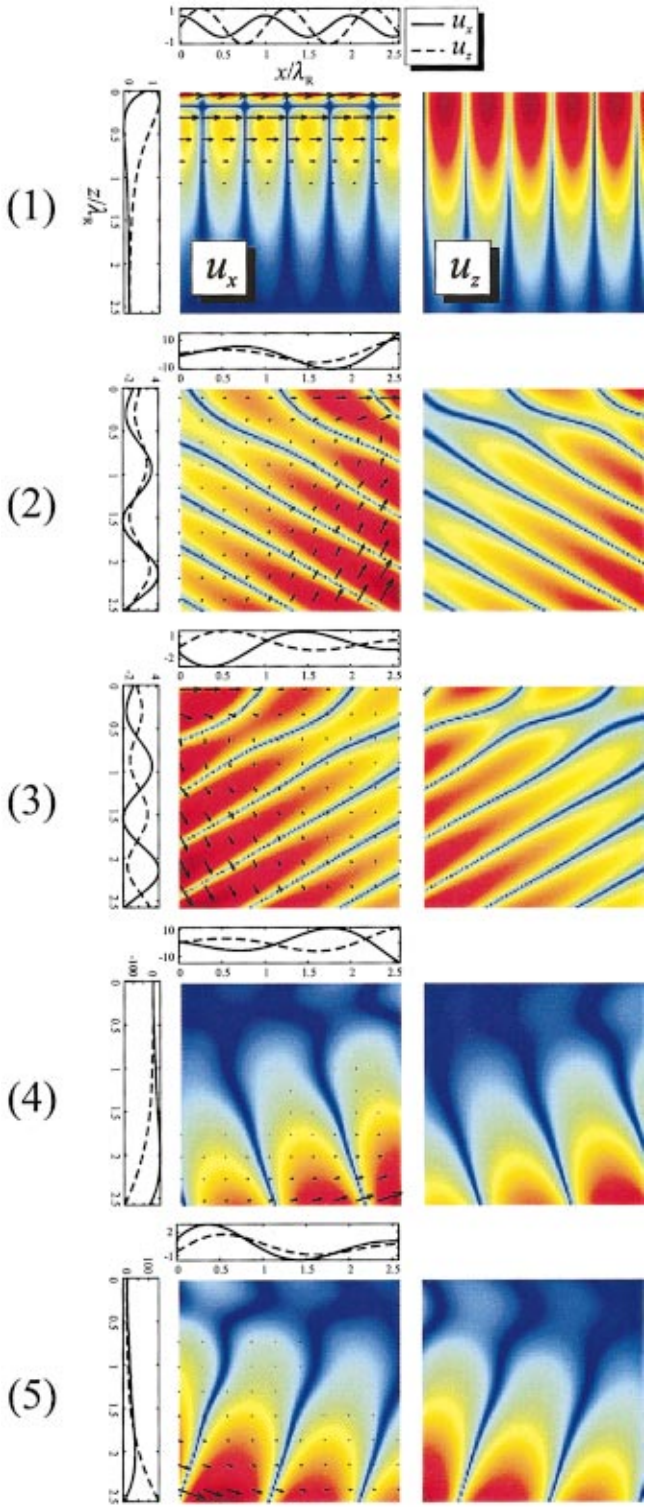

FIG. 2. Horizontal and vertical displacements according to the five solutions of the Rayleigh equation.

of the complex Poynting vector, thus indicating the direction of the energy flow. The upper edge of each plot corresponds to the free surface.

First, the Rayleigh surface wave is shown. For the Rayleigh surface wave, the energy flow is seen to be parallel to the surface. Both the horizontal and the vertical displacements decay away from the surface. The second solution describes a shear wave in which energy is carried toward the surface. Close to the surface, the energy flows parallel to the surface. The waves grow exponentially in the x- and z-direction. The third solution is the converse of the second one. This time, the energy flows from the surface into the medium, and the waves decay in the x-direction. Again, close to the surface the energy flow is parallel to the surface. The fourth and fifth solution are similar to the second and third. However, now a pressure wave propagates in the medium, and the energy flows at a different angle with respect to the surface. Also, the exponential growth is enhanced.

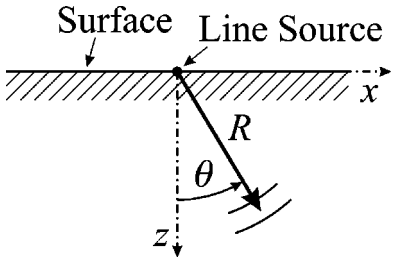

FIG. 3. Line source on the surface.

All of the five possible solutions described above can, in certain cases, represent physical solutions. For example, if a field distribution is created on the surface that matches the field distribution of Solution (5) on the surface, waves similar to the ones described by Solution (5) would be induced in the medium. If a field distribution is generated within the medium that is equal to the field distribution of Solution (2), waves propagating toward the surface would be excited that perfectly couple into a surface wave. Of course, the solutions as described here would require an infinite medium and wave fields of infinite extent that are nonzero at infinity, which violates physical as well as causal constraints. However, over a finite range all of these solutions can be excited with the appropriate field distributions.

IV. WAVES DUE TO A LINE SOURCE ON THE SURFACE

In the previous section, the solutions to the wave equation at a free-surface boundary have been described in a general form. In this section, the wave fields due to a specific excitation, a line source on the surface, are determined. The

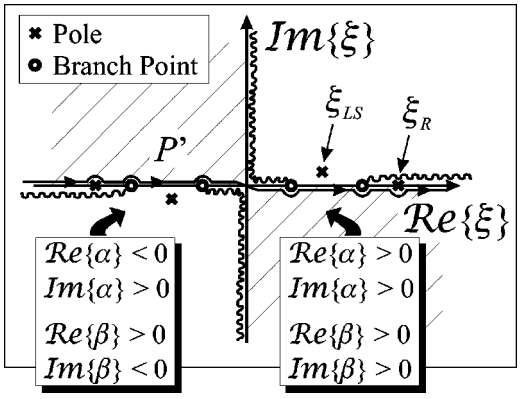

FIG. 4. Location of the poles and branch cuts in the complex ξ-plane for the line-source problem.

analysis presented here is largely based on the general mathematical description of Felsen and Marcuvitz.[9]

Figure 3 shows the underlying geometry. A line source is placed on the surface at $x=0$ and extends into the y-direction. The line source excites the normal stress component τ_{zz}. If harmonic time dependence is assumed, the displacement fields due to a line source can be written in form of an integral equation:[6]

$$u_x(x,z) = -\frac{j}{\mu\pi}\int_{P'}\frac{\xi}{F_0(\xi)} \times[-2\alpha\beta e^{j\beta z}+(\beta^2-\xi^2)e^{j\alpha z}]e^{j\xi x}\,d\xi, \quad (22)$$

$$u_z(x,z) = -\frac{j}{\mu\pi}\int_{P'}\frac{\alpha}{F_0(\xi)} \times[2\xi^2 e^{j\beta z}+(\beta^2-\xi^2)e^{j\alpha z}]e^{j\xi x}\,d\xi, \quad (23)$$

where

$$F_0(\xi) = (\xi^2-\beta^2)^2+4\xi^2\alpha\beta \quad (24)$$

is the Rayleigh equation. The amplitude of the excitation is assumed to be unity.

A. General considerations

The integrals in Eqs. (22) and (23) each represent an inverse Fourier transform from the wave number domain into the spatial domain. The integrands contain poles and branch points. The poles are due to the roots of the Rayleigh equation in the denominator. The branch points arise because of the square root dependence of α and β on ξ. They are located at the roots of α and β, at $k_P=\pm(\omega/c_P)^2$ and $k_S=\pm(\omega/c_S)^2$ [see Eqs. (6) and (7)].

To compute the integrals, contour integration in the complex ξ-plane must be applied. The integration must be performed along the real ξ-axis. Figure 4 shows the location of the poles and branch points in the complex ξ-plane. To determine the waves propagating in the positive x-direction, Eqs. (22) and (23) must be integrated along the path P'. The contour is closed at infinity. Only the poles and branch cuts for $\mathrm{Re}\{\xi\}>0$ are included in the integration contour (indicated by the indentations of P'), whereas the poles for $\mathrm{Re}\{\xi\}<0$ are excluded and, therefore, do not contribute to the integral.

Due to the branch points, the integrands are not single-valued. To make the integrands unique, a Riemann surface for the ξ-plane is necessary, with branch cuts providing the transition from one Riemann sheet to the other.[9] The location of the branch cuts in general is arbitrary, but defines the disposition of those regions in the complex ξ-plane in which for example $\mathrm{Re}\{\alpha\}>0$ or $\mathrm{Re}\{\alpha\}<0$. Figure 4 shows the top Riemann sheet for Eqs. (22) and (23). The signs of the wave numbers on the top Riemann sheet must be chosen according to physical and causal reasons. The integration along the real axis determines the shear and pressure waves excited by the line source. For the shear and the pressure waves to be causal, they must propagate away from the source and vanish at infinity. For this to be true, the wave numbers along the real axis must be chosen such that $\mathrm{Re}\{\alpha\}>0$, $\mathrm{Im}\{\alpha\}>0$, $\mathrm{Re}\{\beta\}>0$ and $\mathrm{Im}\{\beta\}>0$. It can be easily shown that in this case the wave numbers in the entire second and fourth quadrant must behave in the same way. In the first and third quadrant, the branch cuts must then be chosen such that $\mathrm{Re}\{\alpha\}<0$, $\mathrm{Im}\{\alpha\}>0$, $\mathrm{Re}\{\beta\}>0$ and $\mathrm{Im}\{\beta\}<0$. This is true because α and β must be continuous across the real axis. Thus, in the first and third quadrant, the pressure wave potential propagates and increases in the negative z-direction, whereas the shear wave potential propagates and increases in the positive z-direction. It is evident that in the first quadrant of the top Riemann sheet the wave numbers behave as described for Solution (3) of the Rayleigh equation as indicated in Table I. The poles on the top Riemann sheet correspond to physically existing waves and, therefore, the pole associated with Solution (3) of the Rayleigh equation represents a physical solution to the line-source problem. The pole in the third quadrant is the equivalent to the pole in the first quadrant, but describes a wave traveling in the negative x-direction. The two poles on the real ξ-axis are present on all sheets and, consequently, also represent physical waves. All other poles of the Rayleigh equation lie on different sheets and, thus, are nonphysical for the line-source case.

It can be seen in Fig. 4 that four poles and four branch cuts exist on the top Riemann sheet. The poles at $\pm\xi_R$ on the real ξ-axis give rise to the well-known Rayleigh surface wave. The complex poles at $\pm\xi_{\mathrm{LS}}$ in the first and third quadrant describe leaky surface waves propagating to the right and left, respectively. As described earlier, the leaky surface wave couples into a plane shear wave. Both the leaky surface wave and the shear wave that is fed from the surface wave are inhomogeneous, which is indicated by the pole being complex.

B. Steepest-descent approximation

To evaluate the integrals asymptotically in the far field, the method of steepest descent shall be applied. To simplify the procedure, the two terms of the integral are treated separately. Dividing the integrals each into a pressure wave term and a shear wave term, Eqs. (22) and (23) are rewritten as

$$u_x^S(x,z) = -\frac{j}{\mu\pi}\int_{P'}\frac{\xi}{F_0(\xi)}(-2\alpha\beta)e^{j\beta z}e^{j\xi x}\,d\xi, \quad (25)$$

$$u_x^P(x,z) = -\frac{j}{\mu\pi}\int_{P'}\frac{\xi}{F_0(\xi)}(\beta^2-\xi^2)e^{j\alpha z}e^{j\xi x}\,d\xi, \quad (26)$$

$$u_z^S(x,z) = -\frac{j}{\mu\pi}\int_{P'}\frac{\alpha}{F_0(\xi)}2\xi^2 e^{j\beta z}e^{j\xi x}\,d\xi, \quad (27)$$

$$u_z^P(x,z) = -\frac{j}{\mu\pi}\int_{P'}\frac{\alpha}{F_0(\xi)}(\beta^2-\xi^2)e^{j\alpha z}e^{j\xi x}\,d\xi. \quad (28)$$

The total displacements equal the superposition of the pressure wave component and the shear wave component:

$$u_x(x,z) = u_x^S(x,z)+u_x^P(x,z), \quad (29)$$

$$u_z(x,z) = u_z^S(x,z)+u_z^P(x,z). \quad (30)$$

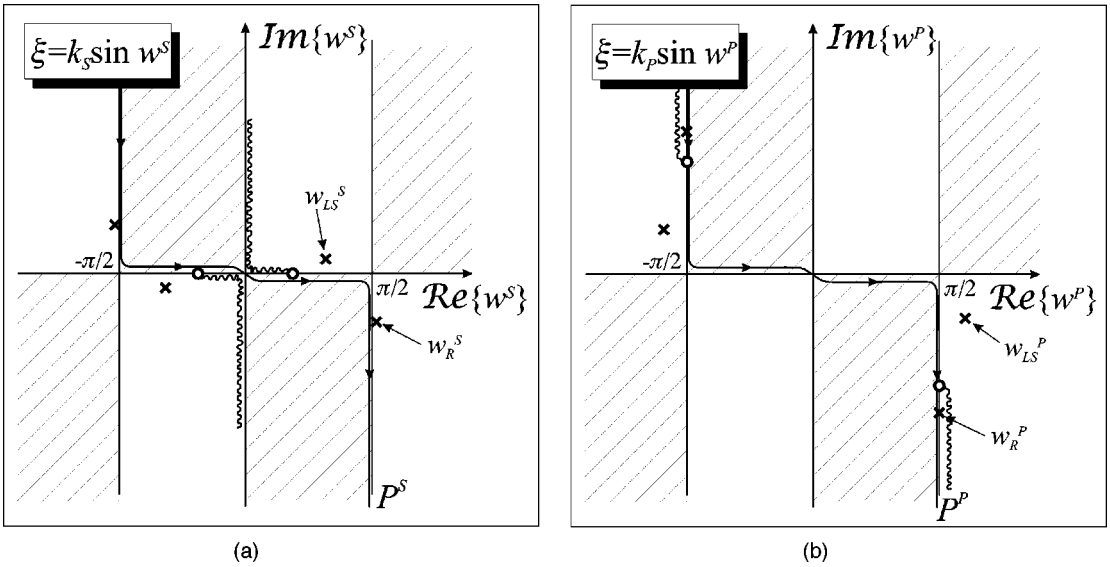

FIG. 5. Location of the poles and branch cuts (a) in the complex w^S-plane and (b) in the complex w^P-plane.

To facilitate the evaluation of the integrals, the complex ξ-plane is transformed into the complex w^S-plane for the two shear wave terms, and into the w^P-plane for the pressure wave terms:

$$\xi = k_S \sin w^S, \tag{31}$$

$$\xi = k_P \sin w^P. \tag{32}$$

These transformations are single-valued.[9] From the periodicity of $\sin w^S$ and $\sin w^P$ it is evident that multiple values for w^S and w^P correspond to a single value of ξ. Thus, the transformations can be used to map the entire ξ-plane with its multiple Riemann sheets into adjacent strips of width 2π in the w^S- or w^P-plane. The arrangement of the poles and branch cuts of the top Riemann sheet in the complex w^S-plane and w^P-plane are shown in Fig. 5. Here, the top Riemann sheet is mapped into a strip reaching from $-\pi$ to π in the complex w^S-plane for the shear wave terms, and similarly for the pressure wave terms in the complex w^P-plane. The positions of the transformed Rayleigh wave pole and the leaky surface wave pole in the complex w^S- and w^P-plane are indicated by w_R^S, w_{LS}^S, and w_R^P, w_{LS}^P, respectively. The transformed integration paths are denoted by P^S and P^P.

The separate transformations for the shear wave terms and the pressure wave terms become necessary, because, when the method of steepest descent is applied, the different terms will give rise to different steepest-descent paths. By applying the different transformations, the steepest-descent paths will have a rather simple shape for both the shear wave

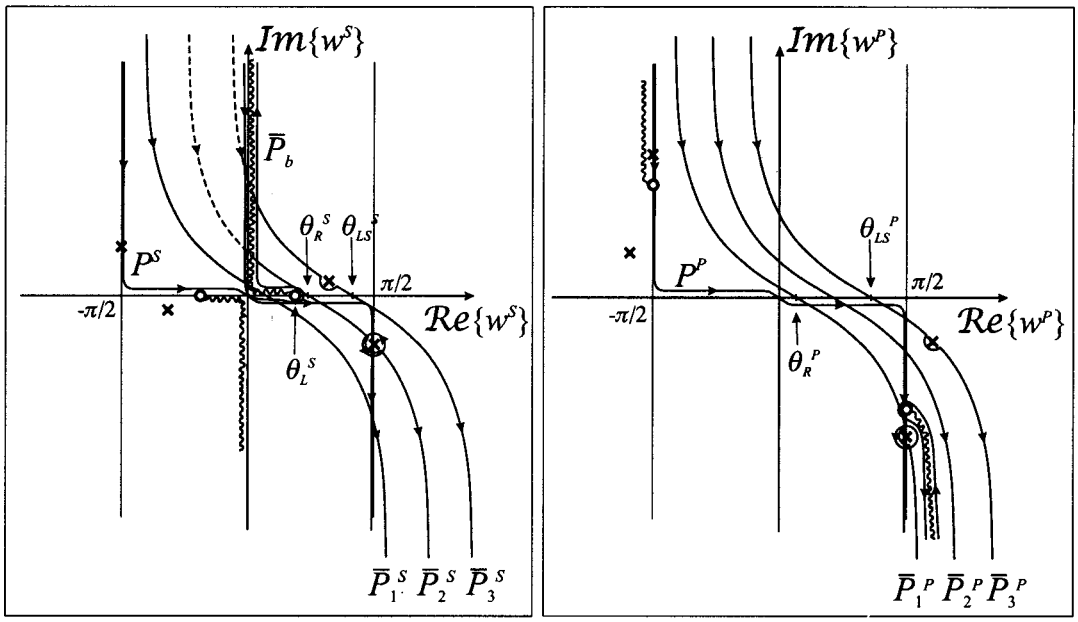

FIG. 6. Steepest-descent paths for (a) the shear wave terms in the complex w^S-plane and (b) the pressure wave terms in the complex w^P-plane.

terms and the pressure wave terms, thus, making the steepest-descent approximation considerably easier.

Applying the transformations, two of the branch cuts are eliminated in each of the integrals in Eqs. (25)–(28). For the shear wave terms the branch cuts at $\pm k_S$ vanish, whereas for the pressure wave terms the branch cuts at $\pm k_P$ are removed. For the shear wave terms, β then reduces to

$$\beta = k_S \cos w^S, \tag{33}$$

and for the pressure wave terms α becomes

$$\alpha = k_P \cos w^P. \tag{34}$$

Introducing polar coordinates,

$$x = R \sin \theta, \tag{35}$$

$$z = R \cos \theta, \tag{36}$$

Eqs. (25)–(28) are rewritten as integrals in the w^S- and w^P-plane:

$$u_x^S(x,z) = -\frac{j}{\mu\pi}\int_{P^S}\frac{\xi}{F_0(\xi)}(-2\alpha\beta) \times e^{jk_S R\cos(w^S-\theta)}\beta\, dw^S, \tag{37}$$

$$u_x^P(x,z) = -\frac{j}{\mu\pi}\int_{P^P}\frac{\xi}{F_0(\xi)}(\beta^2-\xi^2) \times e^{jk_P R\cos(w^P-\theta)}\alpha\, dw^P, \tag{38}$$

$$u_z^S(x,z) = -\frac{j}{\mu\pi}\int_{P^S}\frac{\alpha}{F_0(\xi)}2\xi^2 e^{jk_S R\cos(w^S-\theta)}\beta\, dw^S, \tag{39}$$

$$u_z^P(x,z) = -\frac{j}{\mu\pi}\int_{P^P}\frac{\alpha}{F_0(\xi)}(\beta^2-\xi^2) \times e^{jk_P R\cos(w^P-\theta)}\alpha\, dw^P, \tag{40}$$

where θ describes the polar angle measured from the surface normal toward the propagation direction (see Fig. 3). The wave numbers in terms of w^S are

$$\xi(w^S) = k_S \sin w^S, \tag{41}$$

$$\beta(w^S) = k_S \cos w^S, \tag{42}$$

$$\alpha(w^S) = \pm\sqrt{k_P^2 - \xi(w^S)^2}, \tag{43}$$

and in terms of w^P

$$\xi(w^P) = k_P \sin w^P, \tag{44}$$

$$\beta(w^P) = \pm\sqrt{k_S^2 - \xi(w^P)^2}, \tag{45}$$

$$\alpha(w^P) = k_P \cos w^P. \tag{46}$$

The signs of $\alpha(w^S)$ and $\beta(w^P)$ must be chosen as described earlier for the complex ξ-plane. Thus, in the shaded and nonshaded regions of Fig. 5, α behaves just as in the shaded and nonshaded regions of Fig. 4.

With the integrals transformed as described above, it is relatively straightforward to apply the method of steepest descent. For the method of steepest descent, the integration paths P^S and P^P are deformed into new paths, the *steepest-descent paths* $\overline{P^S}$ and $\overline{P^P}$, respectively. The new path is chosen such that the dominant contribution to the integral arises from only a small section of the path. To achieve this, the path is deformed such that it passes through the saddle point of the integrand. Away from the saddle point it follows the direction in which the integrand decays most rapidly. Along this path, the integrand will then be negligible everywhere but around the saddle point, and the integral can be approximated by the contribution from the integrand in the vicinity of the saddle point.

The path of steepest descent is a path of constant phase.[9] For integrals in the form of the ones in Eqs. (37)–(40), the steepest-descent path is given by

$$\mathrm{Re}\{w^{S,P}\} - \theta = \cos^{-1}(\mathrm{sech}(\mathrm{Im}\{w^{S,P}\})). \tag{47}$$

The procedure is the same for the shear wave terms and the pressure wave terms. In Fig. 6, three steepest-descent paths are shown each for the shear wave terms in the w^S-plane, $\overline{P_1^S}$, $\overline{P_2^S}$, $\overline{P_3^S}$, and for the pressure wave terms in the w^P-plane, $\overline{P_1^P}$, $\overline{P_2^P}$, $\overline{P_3^P}$. Each steepest descent path corresponds to a different propagation (polar) angle. The saddle point in each case is located at the intersection of the steepest-descent path with the real w^S- or w^P-axis, respectively. Physically, the contributions from the saddle points describe the pressure and the shear waves in the far field .

When the original integration path is deformed into the steepest-descent path, care has to be taken whether poles or branch cuts are crossed during the deformation. According to Cauchy's theorem, if a singularity is crossed during the deformation from one integration path into another, the contribution from the contour integral around the singularity must be included into the total integral. For example, when P^S in Fig. 6 is deformed into the steepest-descent path $\overline{P_1^S}$, no singularities are crossed during the deformation. However, for $\overline{P_2^S}$, the integrals around the branch cut, $\overline{P_b}$, and around the pole at w_R^S must be included. For $\overline{P_3^S}$, the branch cut integral as well as the integrals around the poles at w_R^S and w_{LS}^S contribute to the total integral.

The contour integrals around the singularities in both the w^S- and the w^P-plane give rise to different types of waves. The integral around the branch cut in the w^S-plane describes a lateral wave. The lateral wave is a plane shear wave induced by the pressure wave propagating along the surface. It appears only if the polar angle exceeds $\theta_L^S = \sin^{-1}(k_P/k_S)$, because, mathematically, the branch cut integral contributes to the total integral only for $\theta > \theta_L^S$. It can be shown that the integral around the branch cut in the w^P-plane is approximately zero and, thus, it does not contribute to the total integral. The integrals around the poles give rise to the Rayleigh surface wave and the leaky surface wave. They exist only for $\theta > \theta_R^S$ and $\theta > \theta_{\mathrm{LS}}^S$ in the w^S-plane, and for $\theta > \theta_R^P$ and $\theta > \theta_{\mathrm{LS}}^P$ in the w^P-plane. The total Rayleigh surface wave and the total leaky surface wave are comprised of the superposition of the contributions from the integrals around the singularities both in the w^S-plane and w^P-plane. The angles $\theta_R^{S,P}$ and $\theta_{\mathrm{LS}}^{S,P}$ are easily obtained by inserting $w_R^{S,P} = \sin^{-1}(\xi_R/k_{S,P})$ and $w_{\mathrm{LS}}^{S,P} = \sin^{-1}(\xi_{\mathrm{LS}}/k_{S,P})$ into Eq. (47).

The integrals are now approximately determined using the method of steepest-descent. Five separate wave types arise: the bulk shear wave, the bulk pressure wave, the Rayleigh surface wave, the leaky surface wave and the lateral wave. A detailed description of the steepest-descent method is given, for example, by Felsen and Marcuvitz.[9]

Using the method of steepest-descent, the shear wave in the far field comes out to be

$$u_x(R,\theta)|_{\text{Shear}} = \frac{j}{\mu\pi}\sqrt{\frac{2\pi}{k_S R}}\frac{e^{j(k_S R-\pi/4)}}{F_0(k_S \sin\theta)} \cdot 2\sqrt{k_P^2-k_S^2\sin^2\theta}\,k_S^3 \sin\theta\cos^2\theta, \quad (48)$$

$$u_z(R,\theta)|_{\text{Shear}} = \frac{-j}{\mu\pi}\sqrt{\frac{2\pi}{k_S R}}\frac{e^{j(k_S R-\pi/4)}}{F_0(k_S \sin\theta)} \cdot 2\sqrt{k_P^2-k_S^2\sin^2\theta}\,k_S^3 \sin^2\theta\cos\theta. \quad (49)$$

For the pressure wave,

$$u_x(R,\theta)|_{\text{Pressure}} = \frac{-j}{\mu\pi}\sqrt{\frac{2\pi}{k_P R}}\frac{e^{j(k_P R-\pi/4)}}{F_0(k_P \sin\theta)} \cdot [k_S^2-2k_P^2\sin^2\theta]k_P^2 \sin\theta\cos\theta, \quad (50)$$

$$u_z(R,\theta)|_{\text{Pressure}} = \frac{-j}{\mu\pi}\sqrt{\frac{2\pi}{k_P R}}\frac{e^{j(k_P R-\pi/4)}}{F_0(k_P \sin\theta)} \cdot [k_S^2-2k_P^2\sin^2\theta]k_P^2 \cos^2\theta. \quad (51)$$

The Rayleigh surface wave and the leaky surface wave are derived from the contour integral around the respective poles of the Rayleigh equation. Using contour integration, the Rayleigh wave is described by

$$u_x(R,\theta)|_{\text{Rayleigh}} = \frac{2\xi_R}{\mu F_0'|_{\xi_R}}[U(\theta-\theta_R^S) \cdot(-2\alpha_R\beta_R)e^{j\beta_R R\cos\theta} + U(\theta-\theta_R^P) \cdot(\beta_R^2-\xi_R^2)e^{j\alpha_R R\cos\theta}]\cdot e^{j\xi_R R\sin\theta}, \quad (52)$$

$$u_z(R,\theta)|_{\text{Rayleigh}} = \frac{2\alpha_R}{\mu F_0'|_{\xi_R}}[U(\theta-\theta_R^S)\cdot 2\xi_R^2 e^{j\beta_R R\cos\theta} + U(\theta-\theta_R^P)\cdot(\beta_R^2-\xi_R^2)e^{j\alpha_R R\cos\theta}] \cdot e^{j\xi_R R\sin\theta}, \quad (53)$$

where

$$F_0'|_{\xi_R} = 4\xi_R(\xi_R^2-\beta_R^2)+8\xi_R\beta_R\alpha_R-4\xi_R^3\left(\frac{\beta_R}{\alpha_R}+\frac{\alpha_R}{\beta_R}\right). \quad (54)$$

$F_0'|_{\xi_R}$ is the derivative of the Rayleigh equation with respect to ξ at $\xi=\xi_R$, and $U(\theta-\theta_R^{S,P})$ is the Heaviside unit step function; α_R, β_R, and ξ_R describe the wave numbers of the Rayleigh wave (see Table II). The result for the leaky surface wave is determined in exactly the same way and is obtained by simply replacing $\theta_R^{S,P}$, ξ_R, α_R and β_R by $\theta_{\text{LS}}^{S,P}$, ξ_{LS}, α_{LS} and β_{LS}, i.e., inserting the wave numbers for the leaky-wave pole instead of the Rayleigh wave pole.

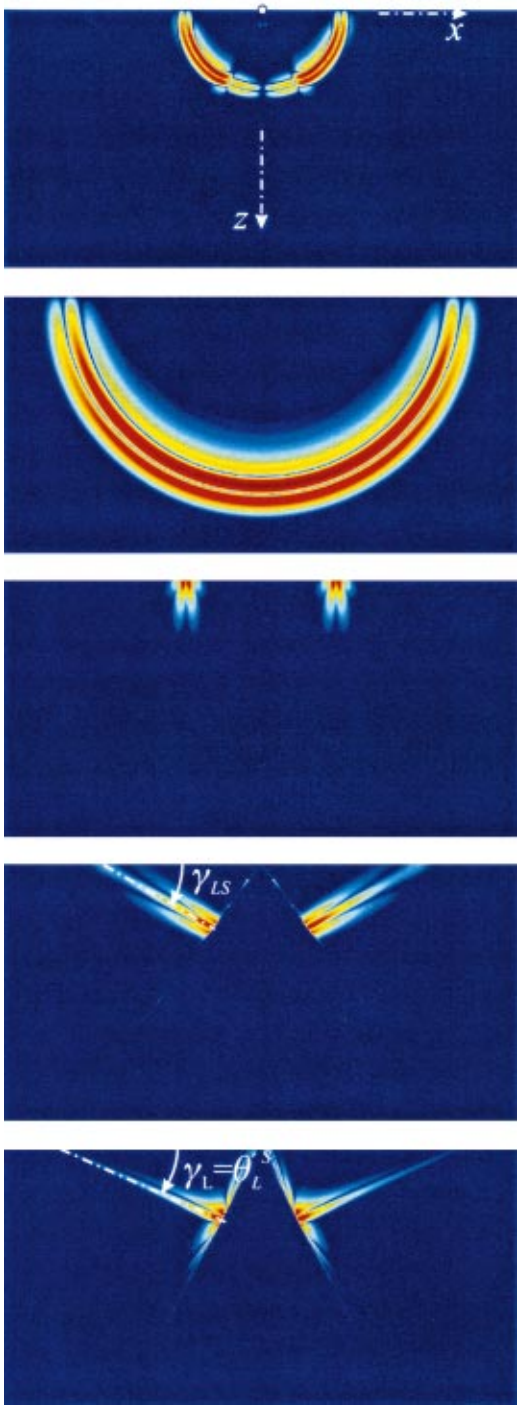

FIG. 7. Waves due to a point source on the surface. From top to bottom: shear wave, pressure wave, Rayleigh surface wave, leaky surface wave, lateral wave.

The lateral wave is defined by the integral around the branch cut, $\overline{P_b}$ in Fig. 6. Following Felsen and Marcuvitz,[9] the integral is asymptotically approximated to become

$$u_x(R,\theta)\big|_{\text{Lateral}} = U(\theta-\theta_L^S)\cdot\frac{-2^{3/2}/(\mu\sqrt{\pi})}{[k_S R|\sin(\theta-\theta_L^S)|]^{3/2}} \cdot\frac{(\sin\theta_L^S)^{3/2}(\cos\theta_L^S)^{5/2}}{(2\sin^2\theta_L^S-1)^2} \cdot e^{jk_S R\cos(\theta-\theta_L^S)+j3/4\pi}, \tag{55}$$

$$u_z(R,\theta)\big|_{\text{Lateral}} = U(\theta-\theta_L^S)\cdot\frac{2^{3/2}/(\mu\sqrt{\pi})}{[k_S R|\sin(\theta-\theta_L^S)|]^{3/2}} \cdot\frac{(\sin\theta_L^S)^{5/2}(\cos\theta_L^S)^{3/2}}{(2\sin^2\theta_L^S-1)^2} \cdot e^{jk_S R\cos(\theta-\theta_L^S)+j3/4\pi}. \tag{56}$$

C. Example

Equations (48)–(56) give the asymptotic far-field approximations for the wave fields excited by a harmonic line source on the surface. To determine the wave fields for a specific excitation in the time domain, the results must be transformed from the frequency domain into the time domain and convolved with the excitation function. The inverse-Fourier transform is given by

$$\hat{\mathbf{u}}(R,\theta,t) = \int_{\omega=-\infty}^{+\infty} G(\omega)\cdot\mathbf{u}(R,\theta,\omega)\cdot e^{-j\omega t}\,d\omega. \tag{57}$$

Here, $G(\omega)$ represents the Fourier transform of the excitation function. To obtain the particle velocity rather than the displacement, the displacement is differentiated with respect to time:

$$\hat{\mathbf{v}}(R,\theta,t) = \int_{\omega=-\infty}^{+\infty} G(\omega)\cdot\mathbf{u}(R,\theta,\omega)\cdot(-j\omega)e^{-j\omega t}\,d\omega. \tag{58}$$

In the following, a differentiated Gaussian pulse is used as excitation, with its Fourier transform

$$G(\omega) = -j\sqrt{2\pi}t_0^2\omega\cdot e^{0.5-0.5(\omega t_0)^2}, \tag{59}$$

where t_0 describes the width of the pulse. The particle velocity is determined here, because the analytical results are to be compared to numerical results, and the numerical finite-difference code that has been developed for this purpose computes the particle velocity rather than the particle displacement.

The wave fields excited by a differentiated Gaussian pulse are computed for a material with a Poisson ratio of $\nu = 0.4$. The wave fields are calculated according to Eqs. (48)–(56) and then transformed into the time domain using Eq. (58). In Fig. 7, the separate wave fields throughout the half

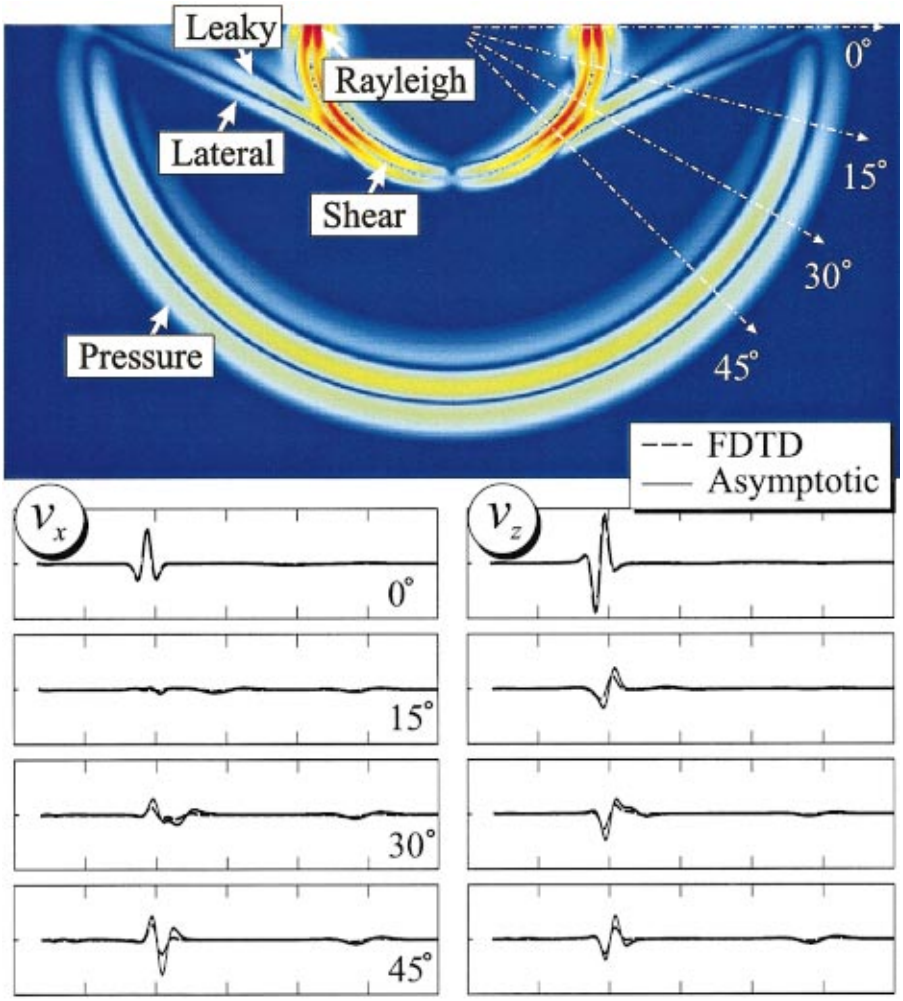

FIG. 8. Finite-difference results; comparison to asymptotic solution.

space are plotted for one instant in time, ten milliseconds after their excitation. The plots show, from top to bottom, the shear wave, the pressure wave, the Rayleigh surface wave, the leaky surface wave, and the lateral wave. A logarithmic color scale is used, ranging from dark red (0 dB) over yellow and green to blue (−40 dB). The top of each plot coincides with the surface of the medium. The source is located on the surface, at the center of each plot.

The shear wave and the pressure wave exhibit cylindrical wave fronts. They both vanish at the surface. The Rayleigh surface wave is confined to the surface and decays into the *z*-direction. The leaky surface wave propagates along the surface with a speed greater than the one of the shear wave, but smaller than the speed of the pressure wave. It feeds an inhomogeneous plane shear wave. The angle that the shear wave makes with the surface is approximately defined by

$$\gamma_{\mathrm{LS}} = \sin^{-1}(\mathrm{Re}\{\xi_{LS}\}/k_S). \tag{60}$$

Due to the coupling into the shear wave, the leaky wave ''leaks'' energy into the medium and decays in its propagation direction. The lateral wave propagates at an angle of approximately

$$\gamma_L = \theta_L^S = \sin^{-1}(k_P/k_S). \tag{61}$$

The artifacts that are especially visible for the lateral wave are due to the Fourier transform algorithm that is being used.

Figure 8 shows the wave fields due to a line source on the surface at one instant in time as determined numerically with the finite-difference time-domain (FDTD) algorithm. The wave fields are plotted at the top on a logarithmic color scale on a cross section through the half space and at the bottom on a linear scale along four radial lines, corresponding to four distinct propagation angles, as a function of the distance from the source. Again, a material with a Poisson ratio of 0.4 is assumed. With careful inspection, the five different wave types are distinguishable. The differences between the FDTD result and the asymptotic approximation are mainly due to the fact that the asymptotic approximation describes the waves in the far field, whereas the FDTD computations show the waves in the near field. Results essentially identical to the FDTD results have been obtained when integrating Eqs. (22) and (23) numerically rather than approximating the integrals asymptotically.[10]

To obtain a better picture of the behavior of the various waves at the surface, the particle motion due to the different surface waves is analyzed. For this, the wave fields of the Rayleigh surface wave, the leaky surface wave and the lateral wave are computed using Eqs. (52)–(56) for harmonic time-dependence, and hodograms of the particle motion at the surface are generated. In these hodograms, the vertical displacement along the surface is plotted versus the horizontal displacement. The hodograms are shown in Fig. 9. As it is well-known, the particle motion due to a Rayleigh surface wave is retrograde (counterclockwise) in nature [Fig. 9(a)]. This is caused by a phase shift between the horizontal and the vertical displacement component: the horizontal displacement is lacking 90 degrees in phase behind. The hodogram also indicates that the Rayleigh wave does not decay as it propagates along the surface. The particle motion

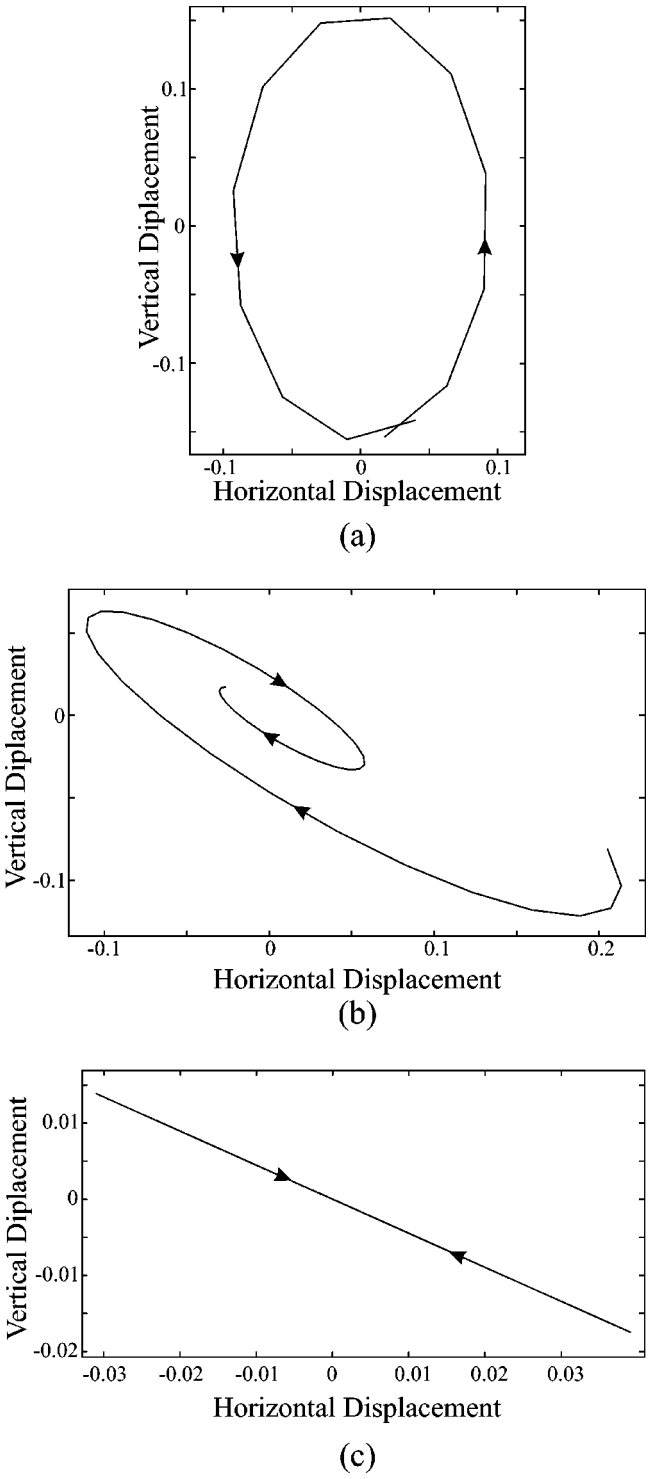

FIG. 9. Hodograms of the particle motion at the surface. Plots for the vertical displacement vs the horizontal displacement for (a) the Rayleigh surface wave, (b) the leaky surface wave, and (c) the lateral wave.

due to the leaky surface wave is prograde (clockwise), caused by the horizontal displacement being ahead in phase of the vertical displacement [Fig. 9(b)]. Clearly, the leaky surface wave decays as it travels along the surface. For the lateral wave, the displacement components are in phase, and the hodogram shows a diagonal line [Fig. 9(c)]. The lateral wave also decays as it propagates along the surface. The prograde and retrograde particle motions of surface waves

have also been observed experimentally by, for example, Smith *et al.*[3]

V. CONCLUSIONS

This paper gives a detailed theoretical description of the existence of a leaky surface wave in an isotropic homogeneous solid. The leaky surface wave is shown to arise from the complex conjugate roots of the Rayleigh equation. It exists only for materials with a Poisson ratio larger than about 0.263. The leaky surface wave propagates along the surface with a wave speed smaller than the pressure wave, but larger than the shear wave. Due to matching tangential wave vectors at the surface, it couples into a plane shear wave directed into the medium. Both the surface wave and the plane shear wave are, because of the coupling, inhomogeneous. It is demonstrated that a normal line source on the surface of an infinite half-space in fact excites the leaky surface wave. The far field expressions for the leaky surface wave are given and are compared to numerical results obtained by using the finite-difference time-domain method. The particle motion on the surface due to the leaky surface wave is prograde (clockwise), contrary to the well-known Rayleigh surface wave which induces a retrograde (counterclockwise) particle motion.

ACKNOWLEDGMENTS

The authors would like to thank Professor Glenn S. Smith, Professor Peter H. Rogers, Dr. Gregg D. Larson, and James S. Martin for their advice and consideration throughout this research and their help in obtaining support for this project. This work is supported in part under the OSD MURI program by the U.S. Army Research Office under Contract No. DAAH04-96-1-0448, and by a grant from the U.S. Office of Naval Research under Contract No. N00014-99-1-0995.

[1] J. W. S. Rayleigh, Proc. London Math. Soc. **17**, 4 (1887).
[2] M. Roth, R. Spitzer, and F. Nitsche, in *Proc. 12th Annu. Int. Meeting, Symp. Application of Geophysics to Engineering and Environmental Problems* (1999), pp. 49–55.
[3] E. Smith, P. S. Wilson, F. W. Bacon, J. F. Manning, J. A. Behrens, and T. G. Muir, J. Acoust. Soc. Am. **103**, 2333 (1998).
[4] N. E. Glass and A. A. Maradudin, J. Appl. Phys. **54**, 796 (1983).
[5] R. A. Phinney, Bull. Seismol. Soc. Am. **51**, 527 (1961).
[6] K. F. Graff, *Wave Motion in Elastic Solids* (Dover, New York, 1975).
[7] J. Miklowitz, *The Theory of Elastic Waves and Wave Guides* (North-Holland, New York, 1978).
[8] J. D. Achenbach, *Wave Propagation in Elastic Solids* (North-Holland, New York, 1973).
[9] L. B. Felsen and N. Marcuvitz, *Radiation and Scattering of Waves* (IEEE Press, 1994).
[10] C. T. Schröder and W. R. Scott, Jr., IEEE Trans. Geosci. Remote Sens. **38**, 1505 (2000).